Solar Physics (2006) 239: 257–276
DOI: 10.1007/s11207-006-0181-7 

# SPATIAL AND TEMPORAL SCALES OF CORONAL MAGNETIC RESTRUCTURING IN THE DEVELOPMENT OF CORONAL MASS EJECTIONS

YAYUAN WEN and JINGXIU WANG
*National Astronomical Observatories, Chinese Academy of Sciences, Beijing 100012, P.R. China (e-mail: yayuanwen@ourstar.bao.ac.cn)*

DALMIRO JORGE FILIPE MAIA
*National Astronomical Observatories, Chinese Academy of Sciences, Beijing 100012, P.R. China; CICGE, Observatório Astronómico Professor Manuel de Barros, Faculdade de Ciências da Universidade do Porto, 4430-146 Vila Nova de Gaia, Portugal*

and

YUZONG ZHANG, HUI ZHAO, and GUIPING ZHOU
*National Astronomical Observatories, Chinese Academy of Sciences, Beijing 100012, P.R. China*

(Received 22 March 2006; accepted 23 October 2006; Published online 1 December 2006)

**Abstract.** It has been commonly accepted that coronal mass ejections (CMEs) result from the restructuring or reconfiguring of large-scale coronal magnetic fields. In this paper, we analyzed four CME events using Nançay Radioheliograph (NRH) images and the experiments onboard the Solar and Heliospheric Observatory (SOHO) spacecraft to understand the coronal restructuring leading to CME initiation. We investigated the onset, duration, and position of the radio emissions in relation to EUV dimming and the inferred CME onset.

It has been identified that the early CME development on the solar disk is characterized by a series of distinct radio bursts. These nonthermal radio sources appeared in phase with coronal dimming shown by SOHO-EIT images and are located within the EUV dimming or ongoing dimming regions. Three time scales are identified: the duration, the separation of individual radio bursts, and the overall time scale of all of the nonthermal sources. They fall in the ranges of approximately tens of seconds to three minutes, one to three minutes, and 15 – 20 minutes, respectively. The individual radio emission seems to shift and expand at the speed of the fast magnetoacoustic waves in the corona; while the nonthermal radio emissions as a whole appear episodically to correspond to the successive coronal restructuring. If we define the triggering speed by dividing the overall spatial scale by the temporal scale of all the radio bursts, then the triggering speed falls in the range of $300 - 400\,\mathrm{km\,s^{-1}}$. This implies that the general process of coronal restructuring and reconfiguring takes place at a speed slower than either the Alvfenic or acoustic speed in the corona. This is a type of speed of "topology waves," *i.e.*, the speed of successive topology changes from closed to open field configuration.

## 1. Introduction

Coronal Mass Ejections (CMEs) are eruptions of large-scale magnetic field and magnetized plasma from the Sun into the heliosphere. Full-halo CMEs that originate on the visible solar hemisphere are often connected with the signatures of large-scale changes seen on the solar disk. Many authors have studied the relationship between

solar surface activity (such as flares and filament eruptions) and CMEs (St. Cyr *et al.*, 1999; Gilbert *et al.*, 2000; Zhang *et al.*, 2001; Gopalswamy *et al.*, 2003; Zhou, Wang, and Cao, 2003). Furthermore, CMEs and flares have been major research subjects in solar physics and space science for decades. But their connections remain one of the outstanding questions in recent years. Flare-CME events have often a much more complex structure than the classical picture of three-component CMEs and involve restructuring of multiple flux systems over a large coronal volume (Aulanier *et al.*, 2000; Delannée, 2000; Maia *et al.*, 2003; Pick, Maia, and Marqué, 2003).

Different density and temperature structures, and therefore different heights in the solar atmosphere, can be probed with observations at different wavelengths (Pohjolainen, 2004). Multiwavelength observations become crucial when we try to analyze activity with an eruptive nature. EUV images tell us about the low-lying cooler loops, magnetograms give us the magnetic connectivity and magnetic flux distribution, and the white-light coronagraph observations provide us the development and propagation of CMEs. Moreover, radio emission is a strong diagnostic in determining whether the emission mechanism is thermal or nonthermal. We can follow the electron propagation paths and coronal shocks by observing the subsequent plasma emission at the local plasma frequency in the surrounding medium at decimetric – metric wavelengths.

Radio observations can be made for both limb and disk events with a higher cadence than coronagraph observations. Recently, radio observations have been an important complementary tool for studying the triggering and development of CMEs. During CME events, nonthermal radio emission is often present and usually masks the thermal emission that has been detected on very rare occasions (Gopalswamy and Kundu, 1992). Radio signatures of flare-CME events correspond to a large variety of bursts, frequently including metric continua (Type IV bursts) that cover a wide frequency range (Gosling *et al.*, 1974; Gopalswamy and Kundu, 1993). Production of shocks during flares or CMEs can also be revealed by the Type II bursts that are produced by the plasma emission mechanism at the local plasma frequency or its harmonics. Type IV radio emission most often occurs in conjunction with Type II emission and has a close association with CMEs (Kahler, 1992).

In this paper, we combine multiwavelength observations and magnetic field extrapolations to estimate the spatial and temporal scales of the coronal magnetic restructuring in the development of the CMEs to understand the physics of CME initiation. The multifrequency Nançay Radioheliograph (NRH; Kerdraon and Delouis, 1997) provides images of the radio bursts in the frequency range of 432 – 164 MHz. Radio observations allow us to follow an event in a large coronal altitude range. The detailed coronal features are obtained by the experiments onboard the Solar and Heliospheric Observatory (SOHO; Domingo, Fleck, and Poland, 1995) spacecraft, *e.g.*, the Large-Angle Spectroscopic Coronagraph (LASCO; Brueckner *et al.*, 1995), and the Extreme Ultraviolet Imaging Telescope (EIT; Delaboudinière *et al.*, 1995). The magnetic configurations are given by the Michelson Doppler Imager

magnetograms (MDI; Scherrer *et al.*, 1995). The radio dynamic spectra are given by IZMIRAN (Gorgutsa *et al.*, 2001) and the Potsdam – Tremsdorf Radiospectrograph (Mann *et al.*, 1992). The X-ray flux comes from the GOES satellites. The flare and the solar radio spectral observations are reported in the Solar Geophysical Data.

Four CME events are selected for this study. They are the events of December 18 2000, April 7 1997, April 6 2004, and June 24 1999. Three of them are associated with only C-class X-ray flares. We have not included too complicated events with the intention of avoiding issues related to the big-event syndrome. Aimed at a thorough understanding of CME initiation, for each event we make careful comparison of the appearance of radio bursts with the EUV dimmings revealed by EIT running- and base-difference images (see Chertok and Grechnev, 2005). To avoid the appearance of false darkening and brightening in the difference images, all of the EIT images are rotated to a common pre-event time. When the same pre-event image is subtracted from all of the subsequent images, the fixed- or base-difference images are reconstructed; while running-difference images are obtained by subtraction of successive images.

The next section of the paper is devoted to the data analysis. We first give a detailed analysis of the event on December 18 2000. Emphasis of the analysis is put on the position and evolution of the distinct radio bursts, their relations with coronal dimmings, and their association with magnetic-flux distribution and connectivity. The other three events share many common properties with the first event. For simplicity and clarity, we describe them in a more abbreviated manner to confirm the conclusions deduced from the first event. Finally, in Section 3, we present the summary and discussion.

## 2. Data Analysis

### 2.1. The December 18 2000 event

#### 2.1.1. *A Brief Introduction*

The complex solar event observed on December 18 2000 is associated with a GOES C7.0 flare (a 1F flare in H$\alpha$ classification). It started at 11:03 UT inside NOAA Active Region (AR) 9269 which was located at N15E01. The flare was associated with a long filament eruption. The long filament lay above the magnetic neutral line between the AR and an extended bipolar region (EBR) seen in the MDI full-disk magnetogram and synoptic chart.

It has been demonstrated that a flare-CME event often appears to be a phenomenon not of a single active region, but involves a large-scale magnetic structure with coupled multiple-flux systems (Wang *et al.*, 2006). An EBR shown by a magnetic synoptic map or full-disk magnetogram represents a large-scale component of solar magnetism. It is formed by merging a few ARs and/or plage regions. EBR

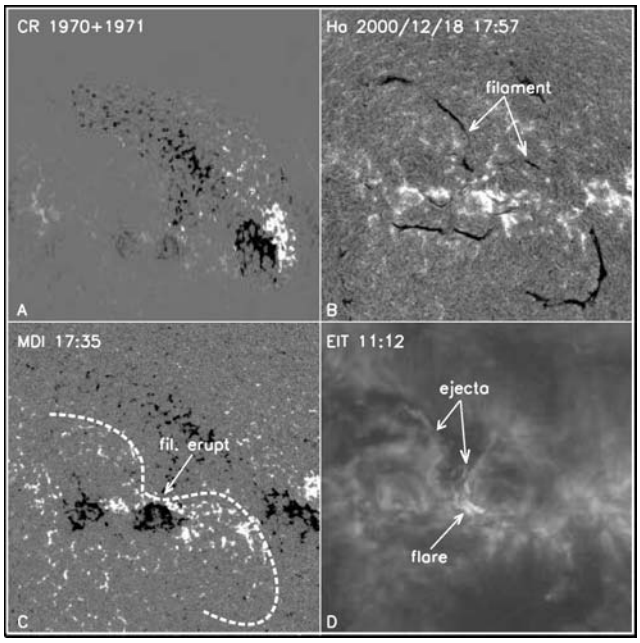


*Figure 1.* *Panel A* is a portion of the MDI synoptic chart in CR 1970 and 1971 showing AR 9269 and an extended bipolar region (EBR). In order to demonstrate the EBR more clearly, the surrounding magnetic structures are artificially weakened. A long filament lay above the magnetic neutral line between the AR and EBR. A BBSO H$\alpha$ image after the filament eruption is shown in *Panel B*. The *dashed line* in *Panel C*, a subset of the MDI daily image, represents the filament position. The *arrows* in *Panel D*, show a subset of an EIT image indicating the bright plasma ejecta and flare ribbons accompanying with the filament eruption. The scale of the synoptic chart is 180 $\times$ 180 heliographic degrees.

appears to be a coherent magnetic structure in the sense that it obeys Hale and Nicholson's polarity law of sunspots for each hemisphere (Hale and Nicholson, 1925). The term refers to Babcock's bipolar magnetic region (Babcock, 1961). Zhou, Wang, and Zhang (2006) find that approximately 36% of Earth-directed halo CMEs in Solar Cycle 23 are associated with EBRs.

In Figure 1, we show the basic magnetic configuration associated with the flare-CME from the MDI magnetogram and synoptic chart. AR 9236 is located to the south of an EBR (see panels A and C). Along the magnetic neutral line, a long filament appeared. Although the flare appeared within AR 9269, it took place during the long filament eruption. Because of the poor temporal resolution of the EIT's observations, we did not see the earliest brightening of the flare. But the bright plasma ejecta associated with the filament eruption and flare ribbons are illustrated very clearly by the EIT image at 11:12 UT. The eruption of the long filament at the boundary of the EBR appears to be an important ingredient of the whole activity. In this sense, the flare as well as the CME are not a single AR phenomenon. The general magnetic structure fits nicely with Category 4 of large-scale CME source

regions of Zhou, Wang, and Zhang (2006) – a long filament on the boundary of an EBR and its associated magnetic fields.

The long filament eruption took place from 11:02 to 11:58 UT, and the GOES flare appeared in the interval of 11:03 to 11:29 UT. The associated CME was first seen in the LASCO C2 field of view at 11:50 UT, with an average projected speed of 510 km $s^{-1}$. A backward extrapolation of the CME front in the LASCO C2/C3 suggests a CME initiation time of 11:14 UT. The time difference between the linear fit and quadratic-fit is about three minutes. However, with the poor temporal resolution of the LASCO observations, the real uncertainty of the estimation cannot be less than 20 – 30 minutes. But with the very high temporal resolution of the Nançay Radioheliograph images, we have identified a group of nonthermal Type II and Type IV radio bursts at 164 MHz from 11:08 UT during the flare and filament eruption. These episodic radio bursts serve as the signature of the early on-disk development of the CME, in addition to the plasma ejecta and EUV dimming revealed by EIT images.

2.1.2. *Position and Flux of Distinct Radio Bursts*

The identification of the radio bursts is based on the analysis of the NRH images obtained at 410, 327, 236, and 164 MHz. By examing the time-lapse radio images with a ten-second cadence, the radio burst on the solar disk can be easily recognized. A radio burst usually expands and shifts continuously at a speed of several hundred km $s^{-1}$. Whenever a jump in position of the radio emission takes place, we will count a new radio burst. The position of each radio burst at each time is determined as the intensity-weighted center of the burst, and its average position is used as the representative position of each burst. For the December 18 event, nine distinct radio bursts are identified. These nonthermal radio bursts took place approximately from 11:08 UT until 11:24 UT. They are shown by a time sequence of NRH images in Figure 2, and marked by the capital letters from "A" to "I" in temporal order.

The position – time plots of the radio emission on the Sun, which are shown in Figure 3, not only greatly facilitate the identification of the individual radio burst, but also illustrate the characteristics of their expansion and placement. The episodic radio bursts are superposed on the enhanced radio continuum. All of the identified radio bursts are marked by the same letters as in Figure 2.

The flux changes of the radio bursts are plotted on the bottom of Figure 3, and the GOES X-ray flux of the flare is superposed on the plot of 164 MHz. The early radio bursts "A," "B," and "C" took place in the impulsive phase of the flare. The strongest radio burst "D" appeared at the maximum of soft X-ray emission. It is a Type II burst. The frequency shift of this Type II burst can be roughly seen from the time difference of the flux profiles from 410 to 164 MHz (see the arrows and the time window marked by the two vertical dashed lines in the figure). All of the other bursts are Type IV in nature. Source "D" is the strongest burst, while source "G" has the longest duration that may contain unseparated subbursts in the current observations. The series of short sporadic bursts only represented a part of

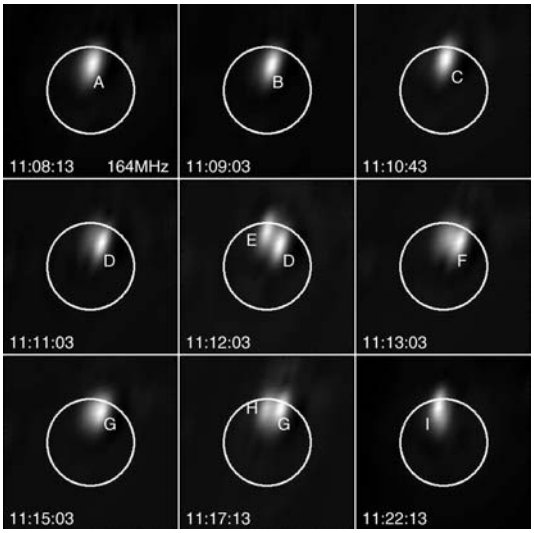


*Figure 2.* NRH images at 164 MHz showing the position and evolution of the radio sources. The successive radio sources are marked by capital letters from "A" to "I."

the long-lasting Type II and Type IV bursts over a broad waveband, associated with the halo CME (see the dynamic radio spectra from IZMIRAN shown in Figure 4).

The episodic radio bursts have an average duration, or lifetime, of 70 seconds. It is measured by the interval of the radio burst with flux higher than its background level. The successive bursts are separated one from another by approximately two minutes.

2.1.3. *Association to Coronal Dimmings*

The flare reached its peak at 11:11 UT (see the flare ribbon in Figure 1 and the GOES light curve in Figure 3). The top two panels of Figure 5 are the EIT images. The saturated patches in the two panels indicate the flare kernels. The diagonal EUV dimming regions are indicated by two arrows (Thompson *et al.*, 1998; Zarro *et al.*, 1999). The next four panels are EIT running- and base-difference images. The dimmings that are near AR 9269 were first seen at 11:11 UT. They extended from the flare site, and moved toward the North.

All of the identified radio sources are denoted by the same capital letters in Figure 5. At 11:08:13 UT, the two weak bursts "A" and "B" were detected. They expanded with the projected velocity of approximate 700 km $s^{-1}$ and 470 km $s^{-1}$, respectively. They appeared at the coronal wave fronts shown by an EIT difference image of 11:11 – 10:59 UT (see Figure 5). Radio bursts "C," "D" appeared at 11:10:33 and 11:11:03 UT, respectively; then, bursts "E" and "F" followed at approximately 11:13 UT. The flux of burst "D" rose abruptly and the source moved toward the northeast, in the expansion direction of the EUV dimming, with an

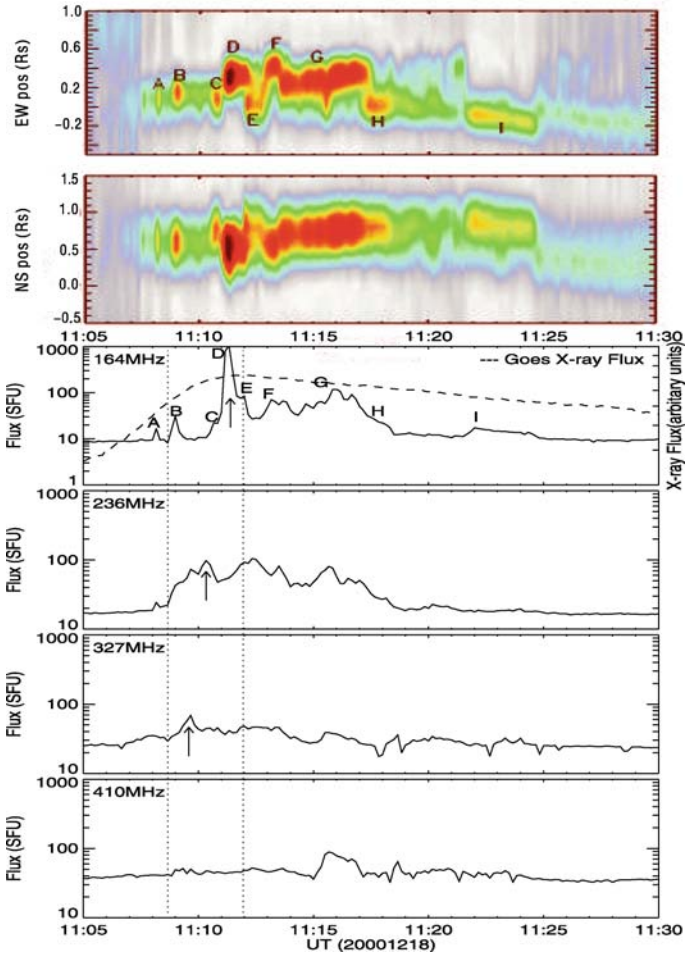


*Figure 3. Top*: The time – position plot shows the expansion and placement of a series of radio-sources identified with letters from "A" to "I" along the East – West and South – North directions, respectively. The colors represent the intensity levels of radio flux. *Bottom*: Flux versus time of the event on the whole Sun at the four frequencies of the NRH. The GOES X-ray flux of the flare is superposed by the *dashed curve*.

initial projected velocity of around 1200 km $s^{-1}$. Finally, we have bursts "G," "H," and "I." Burst "G" is a long-duration source, it moved toward northwest direction with the projected velocity around 650 km $s^{-1}$. This corresponds to the extension of dimming also.

The poor temporal resolution prohibits a definitive statement on whether or not all of the radio bursts appeared at the EUV wave fronts. However, comparing with the time sequence of the base-difference images, we find that the successive appearance of the episodic bursts guided the extension of EUV dimming. It extended

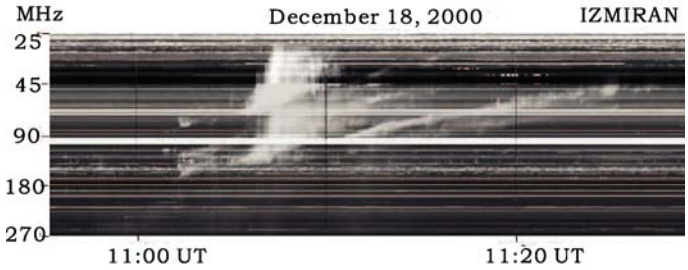


*Figure 4.* Dynamic spectrum from IZMIRAN shows the Type II burst beginning at 11:11 UT. The long continuum is also observed.

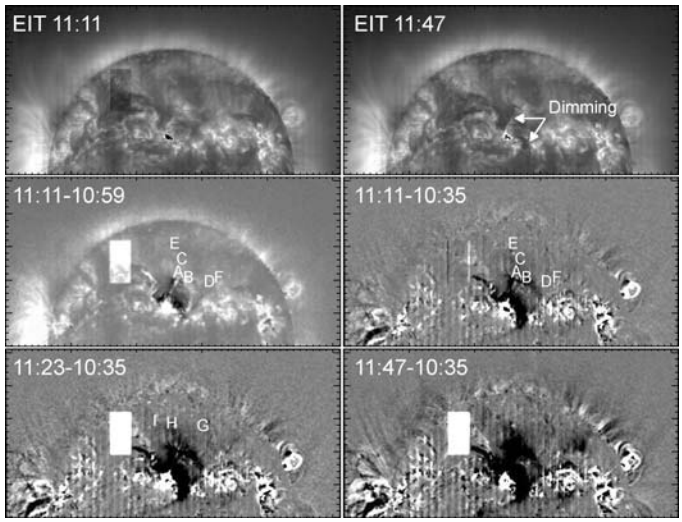


*Figure 5.* The EIT and the EIT running- or base-difference images showing the eruption process of the flare and the development of the larger dimming regions. The positions of radio bursts at 164 MHz are marked by the letters.

first toward the north, then to the northwest, and finally to the northeast. It is likely that each radio burst outlines the EUV wave fronts that represent the coronal shocks.

It is remarkable that, allowing for projection effects, *all of the burst sources are in the dimming regions* (see also the boundary of dimming in Figure 6). The successive appearance of radio bursts generally corresponds to the development of EUV dimming. However, it is worthwhile emphasizing that the radio bursts appeared earlier in the places that were later occupied by EUV dimming. A combined image of EIT and C2 is shown in Figure 6. The figure illustrates clearly that the EUV dimming corresponds very well to the span of the CME seen later in the LASCO C2 field-of-view.

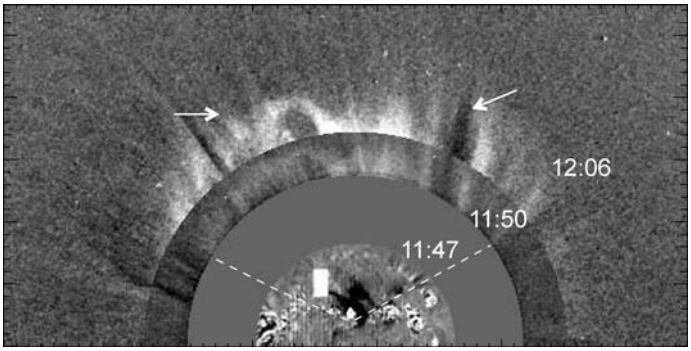


*Figure 6.* The combined image of EIT and C2 shows the EUV dimming corresponding very well to the span of the CME seen later in the LASCO field-of-view. The two *arrows* indicate a loop-like component in the east and an open component in the west, respectively. The *white dashed lines* denote the boundary of the dimmings.

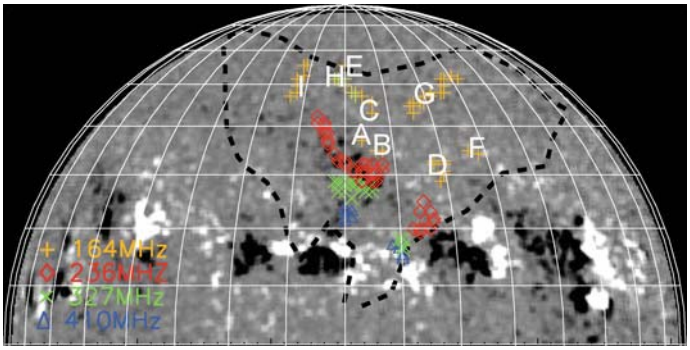


*Figure 7.* The positions of radio bursts at four frequencies are marked on the SOHO-MDI magnetogarm at 09:36 UT on December 18, 2000. The positions of radio sources at the different frequencies are plotted by the different symbols and colors. The *black dashed lines* denote the boundary of the dimming on the disk.

### 2.1.4. *Association with Magnetic Flux Distribution and Connectivity*

To understand the association of the radio bursts with the magnetic-flux distribution and connectivity, all of the identified radio sources are marked by the different symbols on the MDI magnetogram at 09:36 UT in Figure 7 (see also the MDI magnetogram and synoptic chart in Figure 1). To show the large-scale field distribution, the magnetogram has been smoothed by $8 \times 8''$.

The source positions at 164 MHz are higher in altitude than those of other three frequencies, thus may suffer from a more severe projection effect. Matching the radio sources and the magnetic-flux distribution in the photosphere is a rather difficult task. It requires measurements of the vector magnetic field in the corona and the detailed identity of the magnetic connectivity in the solar atmosphere. We might assign the source-projected positions along the local solar radius. However,

the radio sources are necessarily connected vertically to the magnetic fields in the lower atmosphere. Therefore, this does not seem to afford additional arguments on the correlations. Keeping this in mind, the following discussions on the correlation of radio sources and magnetic field distribution are only referring to the gross magnetic structure and are of a tentative nature. Comparing the source positions at higher frequencies helps with understanding the correlations.

AR 9269 was near the Sun's center on the disk. A unipolar region was located on the north of AR 9269. It is the negative component of an EBR. Further to the west, there appeared another EBR. The two weak bursts "A" and "B" are detected in the vicinity of magnetic neutral line of the EBR. Burst "C" appeared in the area of weak positive flux. In roughly coincidence with the maximum of X-ray flux, strong burst "D" appeared close to the magnetic neutral line of two EBRs. The source "E" and "F" appeared at widely separated weak flux regions and the long-duration source "G" appeared above the weak positive flux, while the sources "H" (the color in yellow) and "I" appeared in the weak negative flux region to the northeast. Source "H" was stable, and "I" moved toward the south with the 400 km $s^{-1}$ projected velocity. At the other three frequencies, the radio sources moved toward the northwest, then northeast in coincidence with the EUV dimming. But the movements of these sources are not obvious.

The boundary of the dimming regions are drawn as black dashed lines on the magnetogram. The dimming regions look like a butterfly in shape. The two wings of the butterfly represent the direction of dimming expansion. The west wing is above the unipolar positive magnetic flux, the other is coaligned with the east extension of the EBR. Corresponding with the magnetic flux distribution, the CME appearance in the LASCO C2 (see Figure 6) seems to include an "open" component (the arrow in the west) and a loop-like component (the arrow in the east). The CME span corresponded to the dimming area nicely, and its brightest parts of CME structures were more or less correlated with the distribution of the distinct radio sources.

To identify the magnetic connectivity involved in the radio sources, we compare with the magnetic field extrapolation from a photospheric magnetogram. The potential field line map, calculated by the boundary element method (BEM) with the composite synoptic magnetic map (Wang *et al.*, 2002), is shown in Figure 8. The 3D magnetic lines of force provide clear guidance about the pre-CME magnetic topology of the whole Sun. As the extrapolation is based on the synoptic magnetic chart obtained over one solar rotation, it is not adequate to use the extrapolation to study the CME-associated changes in the Sun's magnetic fields. However, the extrapolated line map shows the topology skeleton of the CME source region clearly.

We projected the radio source positons along the local solar radius. They are denoted by the heads of the arrows in Figure 8. These are used only as references when considering the projection effects in the positions of 164 MHz radio sources. The sources "A" and "B" are located above the magnetic loops connecting positive flux of AR 9269 and negative flux of the EBR. Sources "C," "E," and "H" appear

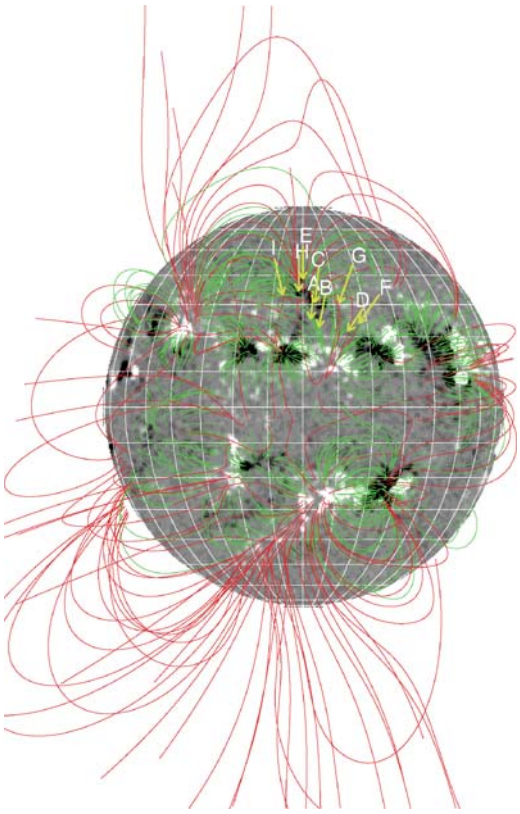


*Figure 8.* The extrapolated magnetic field lines by the boundary element method showing the pre-CME magnetic topology of the whole Sun. The *green lines* represent the closed field lines with height lower than $0.3R_{\odot}$, the *red lines* represent the closed lines with height higher than $0.3R_{\odot}$ and all of the *open field lines*. The positions of radio sources at 164 MHz are marked by the letters. The ends of the *arrows* denote the positions of the radio sources in the line-of-sight projection. The heads of the *arrows* denote the projected positions of the radio sources on the solar surface along the solar radius.

above the magnetic separatrix of seven or eight sets of magnetic loop systems. Each magnetic loop system has one set of footpoints rooted in the separatrix of the negative flux of the EBR, but the other footpoints, widely distributed, cover large range of longitudes and latitudes. "D" lies above a lower-lying loop system connecting AR 9269 and AR 9265 to its West, as indicated by EUV loops in Figure 1. Moreover, this lower-lying loop system seems to cross a midsized loop system connecting the AR flux and the separatrix. "F" is located at the legs of few loop systems including the loop system associated with source "D." Radio source "G" coincides in position with the loop top of middle to large scales, and it is a long-duration Type IV source (see Figure 3); source "I" also correlates with middle or large-scale loop systems. These loop systems are all extended from the common separatrix to widely separated positive flux.

In summary, the majority of the radio bursts appeared in conjunction with many sets of magnetic loop systems, a common separatrix of the negative flux in the EBR. Their locations were closely related to discrete sets of magnetic loop systems.

## 2.2. DESCRIPTION OF THE OTHER THREE EVENTS

### 2.2.1. *The April 7 1997 Event*

The solar event observed on April 7 1997 has been studied by many authors (Sterling and Hudson, 1997; Thompson *et al.*, 1999; Zarro *et al.*, 1999; Sterling *et al.*, 2000; Sterling and Moore, 2004; Aurass *et al.*, 2005). It is associated with a GOES C6.8 flare beginning at 13:54 UT inside NOAA AR 8027. The position of this AR is located at S25E16. The CME associated with this flare was first seen in the LASCO C2 field-of-view at 14:27 UT. The backward extrapolation of the LASCO observations suggests that the CME started at approximately 14:06 UT.

Very similar to the event of December 18 2000, its on-disk development is characterized by the appearance of distinct radio bursts. The six radio bursts observed by the NRH at 164 MHz are marked by letters on Figure 9. The radio source "A" took place since 13:58 UT, in the impulsive phase of the flare. It expanded with the

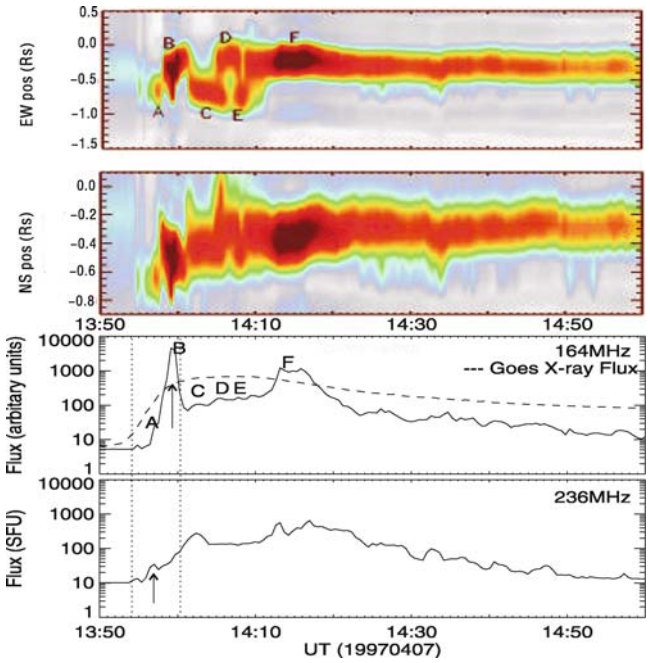


*Figure 9.* The time–position plots and flux versus time of the event on the whole Sun at the two frequencies of the NRH. The GOES X-ray flux of the flare is superposed.

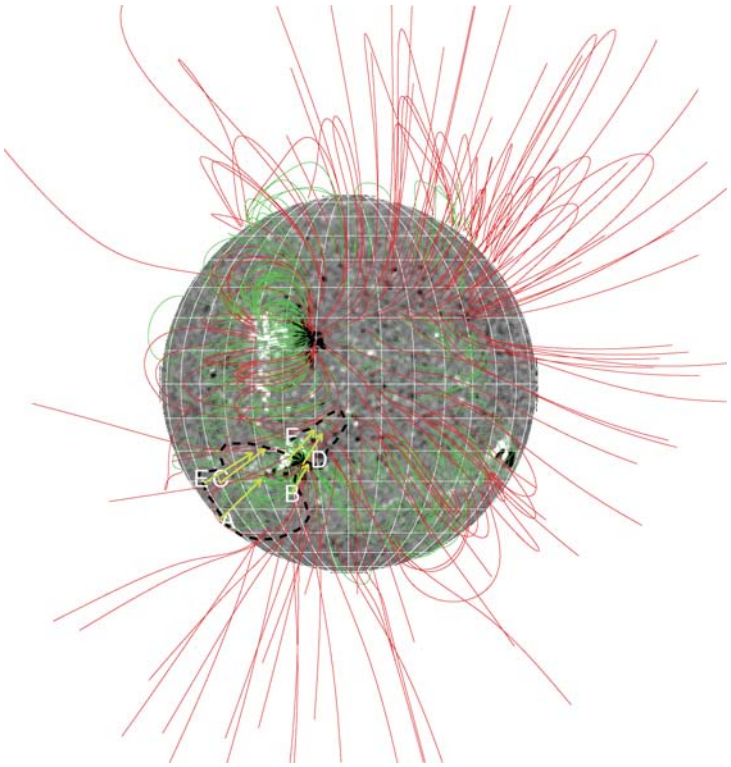


*Figure 10.* The extrapolated magnetic lines show the pre-CME magnetic topology of the whole Sun on April 7 1997. The positions of the radio bursts at 164 MHz are marked by the letters in the same style as in Figure 8.

projected velocity of about 700 km $s^{-1}$. The strongest radio burst ("B") appeared at the maximum of soft X-ray emission, and was Type II in nature. The dynamic spectral observations from the AIP-OSRA in Potsdam (Mann *et al.*, 1992) confirmed the Type II and Type IV bursts beginning around 14:00 UT, and revealed the Type II burst in the wavelength range of 250 – 40 MHz. Each episode in the Type IV burst, "C", "D", "E", and "F", only represents a part of the history of the whole burst. The episodes have an average duration of three minutes, and are separated one from another by approximately two minutes. The overall duration of the episodic bursts is about 21 minutes.

The positions of radio sources at 164 MHz are marked on the magnetic line map in Figure 10. The boundary of EUV dimming regions is drawn as the black dashed lines on the background magnetogram. As in the first event, the successive appearance of radio sources corresponds to the extension of the dimming, and the dimming areas fit well the span of the CME seen later in the LASCO C2 images. There is only one active region, AR 8027, in the Southeast of the Sun within an EBR with negative preceding polarity and positive following polarity (see the

magnetogram in Figure 10). As for the first event, the earliest source "A" was attached to AR loops, and the Type II source "B" lay above a few loop systems from small to midsized. All of the individual radio bursts are found at the legs of discrete magnetic loops. All of the loop systems have one set of footpoints anchored at the negative flux of the EBR where a separatrix can be seen. It is interesting to note that although the EUV waves associated with this event propagated radially from the flare site to a large area on the visible disk (Sterling and Hudson, 1997), a distinct radio burst only appeared in areas with relatively strong fields and many discrete flux loops.

### 2.2.2. *The April 6 2004 Event*

The CME event on April 6 2004 is associated with a GOES M2.4 flare beginning at 12:30 UT inside NOAA AR 10588, which was located at S18E15. The associated CME was first seen in the LASCO C2 field-of-view at 13:31 UT, and extrapolating the LASCO observations suggested it to be initiated at 13:15 UT.

The strong positive flux of the AR was fully embedded in the large amount of negative flux of likely an EBR. Therefore, it is expected that on the boundary of the strong positive flux of the AR there must have been current sheets stretching upward into the high corona. Indeed, Type III bursts were observed by NRH at frequencies of 236 and 164 MHz (see Figure 11) in the impulsive flare phase roughly

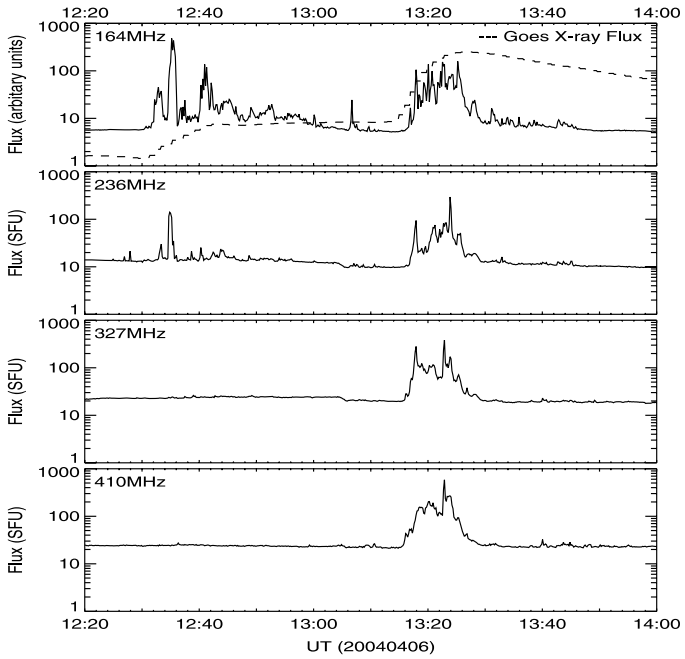


*Figure 11.* Flux versus time of the event on the whole Sun at the different observing frequencies of the NRH. The GOES X-ray flux of the flare is superposed.

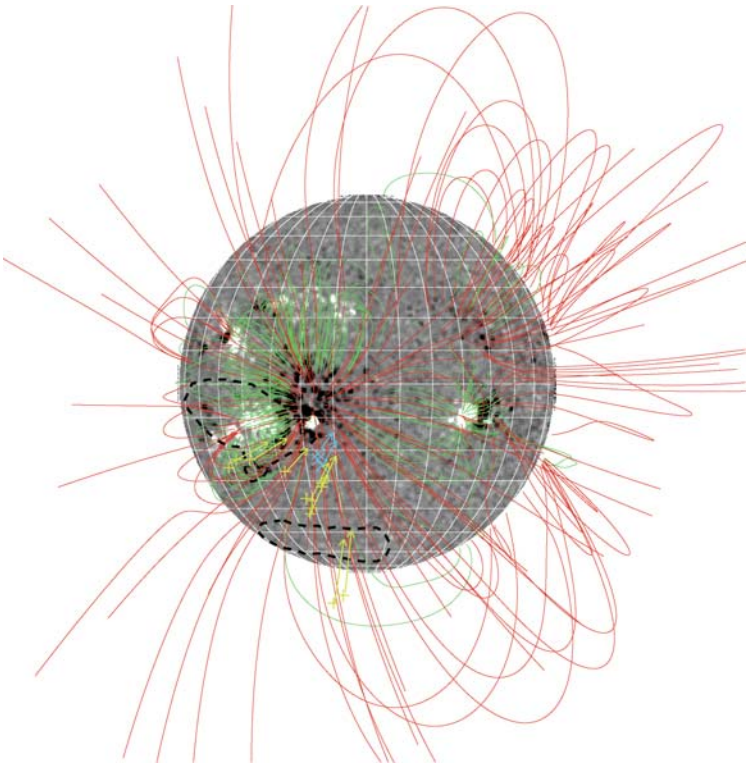

*Figure 12.* The extrapolated magnetic field lines showing the pre-CME magnetic topology of the whole Sun on April 6 2004. The radio sources at 164 MHz are marked on the MDI magnetogram by the different symbols in the same style as in Figure 8. The *yellow plus* denotes the Type IV burst, while the *blue cross* denotes the Type III burst.

from 12:35 UT, indicating magnetic reconnection in the high corona. However, only the new Type IV radio burst started at approximately 13:00 – 13:06 UT, like that reported for the last two events, and is found to be associated with the CME initiation. The weak burst at 13:00 UT appeared in the southeast dimming region (see the black dashed contours in Figure 12), related to the lower- and middle-scale magnetic loop systems connected to the AR 10588. In the figures, we have not distinguished each individual burst, but, at least, three bursts around 13:18, 13:23, and 13:25 UT took place at all four frequencies of the NRH, which indicated deeply-excited sources. Part of the southern coronal hole dimmed, and there was the Type IV burst above the dimmed region too. Moreover, the Type IV radio burst appeared at the site of previous strong Type III bursts above the negative flux surrounding the AR. It is indicative that there were higher magnetic loop systems connecting the southern coronal hole to the negative flux surrounding AR 10588, and the Type IV burst was at the two legs of the large-scale magnetic loops.

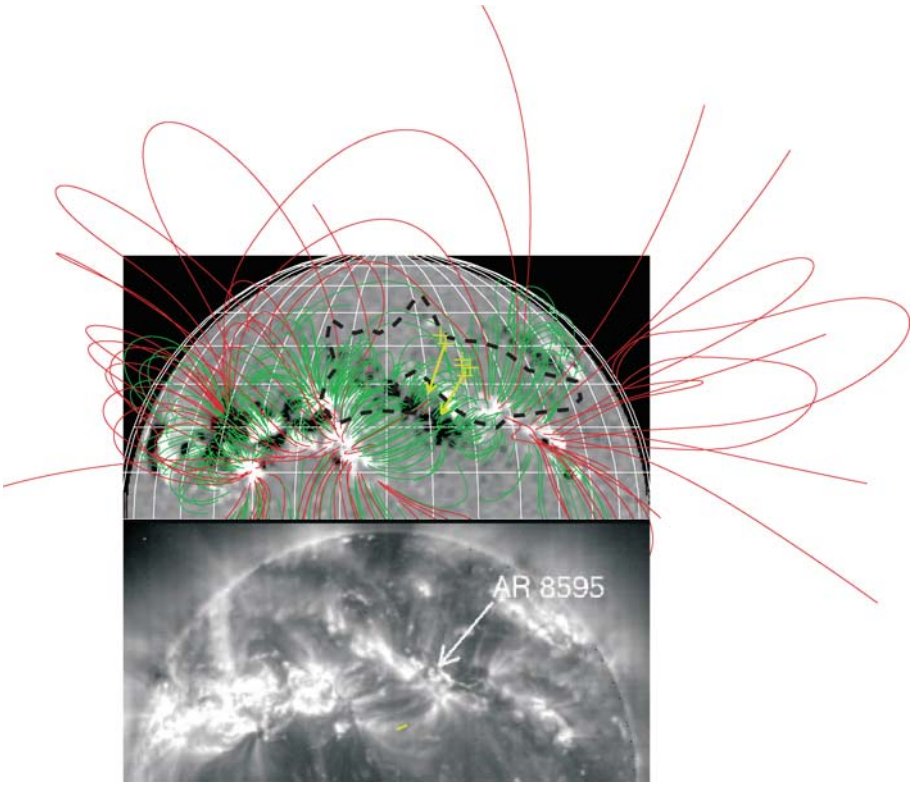


*Figure 13.* In the *upper panel*, the extrapolated magnetic field lines showing the pre-CME magnetic topology of the Sun on June 24 1999. The weak radio sources are marked by the *plus signs* in the same style as in Figure 8. In the *lower panel*, the EIT image shows the eruption of the filament and flare at 13:11 UT.

### 2.2.3. *An Event with Only Weak Radio Bursts*

The CME event observed on June 24 1999 is associated with a long filament eruption within an EBR (see the magnetogram of Figure 13) from 13:11 UT and a long-duration GOES C4.1 flare from 12:04 to 15:10 UT. The CME was first seen in the LASCO C2 field-of-view at 13:31 UT. Tracing back the CME front, it is suggested that the CME started at 13:09 UT, roughly coincided with the long filament eruption. It is worth mentioning that for this event there were no strong Type II or Type IV bursts observed in the frequency range of 40 – 800 MHz. However, weaker radio bursts, very similar in nature to the bursts described in earlier-mentioned three events, were detected during the filament eruption at 164 MHz.

The appearance of weaker radio bursts corresponds well with the extension of coronal dimming, and they are located in the dimming regions. AR 8595 was located in the central part of an EBR, and the long eruptive filament lay above the magnetic neutral line of the EBR also. This large-scale magnetic configuration is

a common condition of CMEs and fits very well with the category C1 (a) of Zhou, Wang, and Zhang (2006). The radio-burst sources seem to lie above the magnetic arcades of the long filament channel of the EBR. The EUV dimmings extended from the magnetic channel to both sides by following the magnetic connectivity with magnetic loop systems. The basic magnetic configuration, dimming, and radio source locations of this event are quite similar to that of the December 18 2000 event, although the radio bursts were so weak. Moreover, the time scale can also be obtained roughly from the EIT images, although the EIT images have a more limited cadence than the radio observations. Presumably, the overall time scale is about 15 – 20 minutes.

## 3. Summary and Discussion

We analyzed four flare-CME events with the emphasis on the early on-disk development of CMEs. The four events selected are all halo CMEs. However, the CME-associated surface activities are different in many perspectives, *e.g.*, the flare significance, radio flux level, and the involvement of filament eruptions. However, a few common properties can be found with regard to the early on-disk development of CMEs.

First, the early on-disk development of CMEs is manifested by the appearance of episodic radio bursts at 164 MHz from Nançay Radioheliograph observations. The total duration of the group of distinct radio bursts is $17 \pm 2$ minutes. Each individual radio burst has an average duration from several tens of seconds to three minutes, and they are separated one from another by an interval of one to three minutes. Most of the radio bursts expand and shift in position at a speed of 700 – 1000 km $s^{-1}$, roughly equal to the speed of local fast magnetoacoustic waves. They first appear in the impulsive phase of the associated flare or early eruption of the associated filament. In two events, the strongest one of the bursts is a Type II burst according to the spectral behavior. The majority of the radio bursts are Type IV in character.

Second, the nonthermal radio bursts are located within the EUV dimming regions, and the successive appearance of the radio bursts seems to presage the extension of the EUV dimming regions. It is likely that the radio bursts tend to appear at the fronts of coronal waves, although the temporal resolution of the EIT observations did not allow a definitive identification. For all four studied CMEs, the location of radio bursts and the dimming region correspond very well to the span of the CME seen from LASCO C2 field-of-view. Coronal dimming is the disk signature of CMEs. It has been demonstrated that the dimming represents the opening of the preclosed magnetic structures and outflow of magnetized plasma (Harra and Sterling, 2001, 2003; Chen *et al.*, 2002). The fact that all the radio bursts were located in the later dimmed regions indicates that radio bursts result from some

types of magnetic interaction, *e.g.*, magnetic reconnection, which then led to the opening and restructuring of the coronal magnetic field. However, it was this series of sporadic radio bursts that characterized the very early development of the CME on the solar disk.

Third, the basic magnetic topology of the EUV dimming region and the radio bursts is the intercoupled multiple magnetic loop system wherein the magnetic source regions are of large spatial scale. An extended magnetic bipolar region (EBR) with either a complex active region or a long filament inside seems to characterize the large-scale characteristics of the source regions. This is consistent with the statistical results found by Zhou, Wang, and Zhang (2006). The location of the radio bursts suggests the conjunction of many sets of magnetic loop systems, or magnetic separatrices.

The overall spatial and temporal scales of the radio bursts seem to characterize the source region and the initiation process of the CME. We define the CME triggering speed by dividing the spatial scale by the time scale. For the four studied CMEs, the triggering speed falls in the range of $300-400\,\mathrm{km\,s^{-1}}$. This triggering speed is less than either the Alfvenic or acoustic speed in the corona. The time scale and the triggering speed identified from our analysis may represent the behavior of magnetic restructuring, *e.g.*, breaking and opening, which results in the eruption of magnetized plasma from previously closed magnetic structures. Therefore, the CME triggering process is not a wave phenomenon, but includes the interaction among individual flux loop systems, as well as, the interaction between loop systems and shock fronts propagated from the CME initiation site. The triggering speed represents how fast the magnetic topology changes from closed to open-field configuration in the CME source regions. In this sense, we might regard the triggering speed as the speed of "topology waves."

To understand the magnetic nature of the radio bursts, for the first time we assign the individual radio burst in the extrapolated magnetic field map and correlate them with the magnetic flux distribution and topology connectivity. An extended magnetic bipolar region (EBR) with either a complex AR, or a long filament inside is the common feature of the source region for all four events. The majority of the radio bursts tend to appear at the conjunction of many sets of flux loop systems, or magnetic separatrices. Only a few radio bursts are identified with individual loop systems. Thus, the initiation of CMEs includes the successive triggering by the reconnection or interaction of individual magnetic loops in an intercoupled flux system.

The radio burst "D" in the December 18 2000 event and "B" in the April 7 1997 are identified to be Type II bursts. The EIT observations and the extrapolated magnetic field maps provide clear hints of the close association of the Type II exciter and the shock ahead of the coronal transient caused by flares.

In one event, a strong Type III burst is identified. However, it is not correlated with the CME initiation. The Type III burst appeared only in the high corona, indicating magnetic reconnection in the stretching current sheet above the strong

positive flux of AR, embedded in the large amount of negative flux. It is likely that only the Type IV burst, which appeared in a large area and represented a large-scale magnetic restructuring, is closely associated with the CME initiation. Interestingly, the early Type III burst in this event has no any observable signature in EIT observations. Only the later Type IV burst shows up by EUV dimmings.

This work supports the suggestion by Pick *et al.* (1998) that the sudden increase of radio emission is associated with one interaction between two systems of loops. These successive interactions lead to magnetic reconnection, then to a large-scale coronal restructuring in the whole CME source region. This is also consistent with the results that the sites of radio emission (tracers of electron acceleration) tend to follow the path of the coronal shock and are located where the shocks encountered magnetic structures and triggered reconnection (Maia *et al.*, 1999; Pohjolainen *et al.*, 2001).

The current work demonstrates that radio imaging observations provide a powerful tool to learn about CME initiation and prediction. By combining the radio-imaging data, the magnetogram, and the theoretical extrapolation, as well as the EUV and X-ray observations, we may have a better understanding of the CME phenomenon, the source regions, initiations, and development.

## Acknowledgements

We thank the Nançay Radioheliograph team for providing the image data. We also thank the SOHO/LASCO, SOHO/MDI, SOHO/EIT teams, IZMIRAN, and Potsdam – Tremsdorf groups for providing the images and dynamic spectra used in the study. We are indebted to MSSL for giving us the facilities to access the various data. We are very grateful to Dr. Karl-Ludwig Klein for kindly reading the manuscript and giving us valuable advice. This work is supported by the National Natural Science Foundation of China (10233050, 10573025, and 40674081).

## References

Aulanier, G., DeLuca, E.E., Antiochos, S.K., McMullen, R.A., and Golub, L.: 2000, *Astrophys. J.* **540**, 1126.
Aurass, H., Rausche, G., Mann, G., and Hofmann, A.: 2005, *Astron. Astrophys.* **435**, 1137.
Babcock, H.W.: 1961, *Astrophys. J.* **133**, 572.
Brueckner, G.E., Howard, R.A., Koomen, M.J., *et al.*: 1995, *Solar Phys.* **162**, 357.
Chen, P.F., Wu, S.T., Shibata, K., and Fang, C.: 2002, *Astrophys. J.* **572**, L99.
Chertok, I.M. and Grechnev, V.V.: 2005, *Solar Phys.* **229**, 95.
Delaboudinière, J.-P., Artzner, G.E., Brunaud, J., *et al.*: 1995, *Solar Phys.* **162**, 291.
Delannée, C.: 2000, *Astrophys. J.* **545**, 512.
Domingo, V., Fleck, B., and Poland, A.I.: 1995, *Solar Phys.* **162**, 1.
Gilbert, H.R., Holzer, T.E., Burkepile, J.T., and Hundhausen, A.J.: 2000, *Astrophys. J.* **537**, 503.

Gopalswamy, N. and Kundu, M.R.: 1992, *Astrophys. J.* **390**, L37.
Gopalswamy, N. and Kundu, M.R.: 1993, *Solar Phys.* **143**, 327.
Gopalswamy, N., Shimojo, M., Lu, W., Yashiro, S., Shibasaki, K., and Howard, R.A.: 2003, *Astrophys. J.* **586**, 562.
Gorgutsa, R.V., Gnezdilov, A.A., Markeev, A.K., and Sobolev, D.E.: 2001, *Astron. Astrophys. Trans.* **20**, 547.
Gosling, J.T., Hildner, E., MacQueen, R.M., Munro, R.H., Poland, A.I., and Ross, C.L.: 1974, *J. Geophys. Res.* **79**, 4581.
Hale, G.E. and Nicholson, S.B.: 1925, *Astrophys. J.* **62**, 270.
Harra, L.K. and Sterling, A.C.: 2001, *Astrophys. J.* **561**, L215.
Harra, L.K. and Sterling, A.C.: 2003, *Astrophys. J.* **587**, 429.
Kahler, S.W.: 1992, *Ann. Rev. Astron. Astrophys.* **30**, 113.
Kerdraon, A. and Delouis, J.: 1997, in G. Trottet (ed.), *Coronal Physics from Radio and Space Observations,* Springer-Verlag, Berlin, p. 192.
Maia, D., Vourlidas, A., Pick, M., Howard, R., Schwenn, R., and Magalhães, A.: 1999, *J. Geophys. Res.* **104**, 112507.
Maia, D., Aulanier, G., Wang, S.J., Pick, M., Malherbe, J.-M., and Delaboudinière, J.-P.: 2003, *Astron. Astrophys.* **405**, 313.
Mann, G., Aurass, H., Voigt, W., and Paschke, J.: 1992, in C. Mattok (ed.), *Coronal Streamers, Goronal Loops, and Coronal and Solar Wind Composition*, ESA-SP-348, Paris, p. 129.
Pick, M., Maia, D., and Marqué, Ch.: 2003, *Adv. Space Res.* **32**, 467.
Pick, M., Maia, D., Kerdraon, A., Howard, R., Brueckner, G.E., Michels, D.J., Paswaters, S., Schwenn, R., Lamy, P., Llebaria, A., Simnett, G., Lanzerotti, L.J., and Aurass, H.: 1998, *Solar Phys.* **181**, 455.
Pohjolainen, S.: 2004, in A.V. Stepanov, E.E. Benevolenskaya, and A.G. Kosovichev (eds.), *Proceedings of the IAU Symposium 223: Multi-Wavelength Investigations of Solar Activity,* Cambridge University Press, Cambridge, UK, p. 329.
Pohjolainen, S., Maia, D., Pick, M., Vilmer, N., Khan, J.I., Otruba, W., Warmuth, A., Benz, A., Alissandrakis, C., and Thompson, B.J.: 2001, *Astrophys. J.* **556**, 421.
Scherrer, P.H., Bogart, R.S., Bush, R.I., *et al.*: 1995, *Solar Phys.* **162**, 129.
St. Cyr, O.C., Burkepile, J.T., Hundhausen, A.J., and Lecinski, A.R.: 1999, *J. Geophys. Res.* **104**, 12493.
Sterling, A.C. and Hudson, H.S.: 1997, *Astrophys. J.* **491**, L55.
Sterling, A.C. and Moore, R.L.: 2004, *Astrophys. J.* **602**, 1024.
Sterling, A.C., Hudson, H.S., Thompson, B.J., and Zarro, D.M.: 2000, *Astrophys. J.* **532**, 628.
Thompson, B.J., Plunkett, S.P., Gurman, J.B., Newmark, J.S., St. Cyr, O.C., and Michels, D.J.: 1998, *Geophys. Res. Lett.* **25**, 2465.
Thompson, B.J., Gurman, J.B., Neupert, W.M., Newmark, J.S., Delaboudinière, J.-P., St. Cyr, O.C., Stezelberger, S., Dere, K.P., Howard, R.A., and Michels, D.J.: 1999, *Astrophys. J.* **517**, L151
Wang, T.J., Yan, Y.H., Wang, J.L., Kurokawa, H., and Shibata, K.: 2002, *Astrophys. J.* **572**, 580.
Wang, J.X., Zhou, G.P., Wen, Y.Y., Zhang, Y.Z., Wang, H.N., Deng, Y.Y., Zhang, J., and Harra, L.K.: 2006, *Chin. J. Astron. Astrophys.* **6**, 247
Zarro, D.M., Sterling, A.C., Thompson, B.J., Hudson, H.S., and Nitta, N.: 1999, *Astrophys. J.* **520**, L139.
Zhang, J., Dere, K.P., Howard, R.A., Kundu, M.R., and White, S.M.: 2001, *Astrophys. J.* **559**, 452.
Zhou, G.P., Wang, J.X., and Cao, Z.L.: 2003, *Astron. Astrophys.* **397**, 1057.
Zhou, G.P., Wang, J.X., and Zhang, J.: 2006, *Astron. Astrophys.* **445**, 1133.